Ann. Geophys., 28, 1961–1979, 2010
www.ann-geophys.net/28/1961/2010/
doi:10.5194/angeo-28-1961-2010

Annales Geophysicae

Radar detection of a localized 1.4 Hz pulsation in auroral plasma, simultaneous with pulsating optical emissions, during a substorm

R. Cosgrove[1], M. Nicolls[1], H. Dahlgren[2], S. Ranjan[3,*], E. Sanchez[1], and R. Doe[1]

[1]Center for Geospace Studies, SRI International, Menlo Park, CA, USA
[2]Space and Plasma Physics, Royal Institute of Technology (KTH), Sweden
[3]Center for Geospace Studies, SRI International, Menlo Park, CA, USA
[*]currently at: Massachusetts Institute of Technology, Cambridge, MA, USA

Received: 30 March 2010 – Revised: 11 October 2010 – Accepted: 11 October 2010 – Published: 29 October 2010

Abstract. Many pulsating phenomena are associated with the auroral substorm. It has been considered that some of these phenomena involve kilometer-scale Alfvén waves coupling the magnetosphere and ionosphere. Electric field oscillations at the altitude of the ionosphere are a signature of such wave activity that could distinguish it from other sources of auroral particle precipitation, which may be simply tracers of magnetospheric activity. Therefore, a ground based diagnostic of kilometer-scale oscillating electric fields would be a valuable tool in the study of pulsations and the auroral substorm. In this study we attempt to develop such a tool in the Poker Flat incoherent scatter radar (PFISR). The central result is a statistically significant detection of a 1.4 Hz electric field oscillation associated with a similar oscillating optical emission, during the recovery phase of a substorm. The optical emissions also contain a bright, lower frequency (0.2 Hz) pulsation that does not show up in the radar backscatter. The fact that higher frequency oscillations are detected by the radar, whereas the bright, lower frequency optical pulsation is not detected by the radar, serves to strengthen a theoretical argument that the radar is sensitive to oscillating electric fields, but not to oscillating particle precipitation. Although it is difficult to make conclusions as to the physical mechanism, we do not find evidence for a plane-wave-like Alfvén wave; the detected structure is evident in only two of five adjacent beams. We emphasize that this is a new application for ISR, and that corroborating results are needed.

Keywords. Ionosphere (Auroral ionosphere; Ionosphere-magnetosphere interactions) – Magnetospheric physics (Storms and substorms)

Correspondence to: R. Cosgrove
(russell.cosgrove@sri.com)

1 Introduction

1.1 Background

Substorm expansion phase onset is thought to be associated with Alfvénic aurora (identified by in-situ satellite measurements (e.g., Mende et al., 2003a, b; Lysak and Song, 2008)), and is normally accompanied by Pi1B magnetic pulsations (Lessard et al., 2006), which continue through the recovery phase. The Pi1B pulsations, which are ground based magnetometer signatures, reflect ionospheric currents averaged over hundreds of kilometers, whereas the Alfvénic aurora are thought to be structured on scales of a few kilometers, or less (Chaston, 2003). Pulsating aurora with periods from a few seconds to tens of seconds are observed optically during the recovery phase, and are often accompanied by more rapid brightness modulations (rapid modulations) with periods that are a fraction of a second (Sato et al., 2004), which is still longer than the periods associated with flickering aurora. Flickering aurora are kilometer-scale patches or columns of emissions sometimes observed by ground based imagers, which oscillate with frequencies from a few Hz to a few tens of Hz (e.g., Whiter et al., 2008). Although the relationship among these various pulsating phenomena is not known, it seems likely that some are related to wave activity in the auroral plasma with associated oscillating electric fields.

In this work we have used the Poker Flat incoherent scatter radar (PFISR) to search for signatures of oscillating electric fields in auroral plasma that might tie some of these phenomena more solidly to wave activity, and thereby to each other. We have discovered that clear radar signatures are difficult to find. However, we have found at least one statistically significant signature. This signature occurred during a period of pulsating aurora, which displayed a very similar spectral

peak in the optical emissions associated with the rapid modulations. However, because there was not a one-to-one correspondence of the optical and radar signatures, the relationship between them is left as a question for future research.

Incoherent scatter radars (ISRs) have a beam width of about 1 km, so that by using the multi-beam capability of the phased-array AMISR (Advanced Modular Incoherent Scatter Radar) radars, it may be possible to probe the kilometer-scale structure of pulsating phenomena. For frequencies above a few tenths of a Hz it is often possible to attribute modulation of the ISR back scatter to something other than modulation of the auroral precipitation (the argument proceeds through the recombination time scale), with oscillating electric fields being the most notable suspect. Oscillating electric fields can modulate ISR back scatter through plasma heating. Divergent oscillating electric fields can modulate the ISR back scatter by modulating the plasma density. Although there are other possibilities, detection of an oscillating ISR signal in the Pc 1 band (0.2–5 Hz) can typically be attributed to oscillating electric fields.

Such electric field probing is complementary to optical observations of pulsations, which imply modulation of the particle precipitation. Optical observations say nothing about the ionospheric electric field. If kilometer-scale electric field oscillations can be detected by ISR, it should provide a valuable analysis tool for study of the relationship of Alfvénic aurora, Pi1B magnetic pulsations, pulsating aurora, flickering aurora, and substorm onset, to wave activity in the auroral plasma. In addition, if some of these phenomena can be related to wave activity, then it may be possible to invoke theoretical models involving the electrical coupling of the magnetosphere and ionosphere (M-I).

There is at least one M-I coupling model that might be evaluated by a radar-based study of pulsations. The ionospheric Alfvén resonator (IAR) (e.g., Polyakov and Rapoport, 1981; Lysak, 1988; Belyaev et al., 1999; Vogt, 2002) and the ionospheric feedback instability (IFI) (e.g., Atkinson, 1970; Sato, 1978; Trakhtengertz and Feldstein, 1984; Lysak, 1986, 1988) together form a foundational M-I coupling model that seeks to explain auroral plasma structuring as a consequence of feedback between ionospheric density modulation, and Alfvén waves resonant in a cavity formed by the ionosphere and the auroral acceleration region (AAR), within the Pc 1 frequency band. In its simplest form, this instability has unstable modes that are waves propagating perpendicular to the geomagnetic field ($\boldsymbol{B}$) with wavelengths of a couple of kilometers or less, and standing along the magnetic field with wavelengths of a thousand to tens of thousands of kilometers. Simulations (Streltsov and Lotko, 2003, 2004, 2008) taking into account gradients and other effects have expanded the range of unstable wavelengths in the perpendicular direction to greater than 10 km. When detected from the ground, these waves should produce density and electric potential structures which oscillate with frequency in the Pc 1 band. In addition, at magnetospheric altitudes the unstable modes comprise inertial Alfvén waves, which support parallel electric fields that accelerate charged particles. These accelerated particles should precipitate into the ionosphere with a temporally oscillating signature (when detected optically – but not, we argue below, when detected by radar).

For example, this instability may come into play at the poleward edge of the substorm auroral surge onset, where intense wave activity and wave accelerated particles (i.e., Alfvénic aurora) have been observed (Mende et al., 2003a, b). More generally, it seems an appropriate hypothesis that waves associated with M-I feedback may be responsible for some of the pulsating phenomena mentioned above, where the theory is not yet developed. If the kilometer-scale structure of electric field modulations associated with pulsations can be probed by ISR, then they can be compared with and used to advance M-I coupling models. The measured wavelength versus frequency characteristic can be compared with the linear dispersion relation for the IFI (most recently, Pokhotelov et al., 2001; Cosgrove and Doe, 2010), and with the simulations by Streltsov and Lotko (2003, 2004, 2008). It can be determined if the effects respect the theoretical thresholds for instability, in terms of the background electric field, the ionospheric conductivity, and in the case of the simulations, the conductivity gradient. The radar can potentially detect the oscillating electric field, whereas optical imagers are specifically sensitive to the effects of charged particle precipitation.

This study is, as far as is known to the authors, the first attempt at applying ISR to these tests. The purpose of this study is to determine whether pulsations in the Pc 1 frequency range (up to 2 Hz) can be detected in PFISR back scatter, and to investigate the possibility that any detections can be attributed to wave activity. This requires that we establish the statistical significance of any detection that we make.

With this in mind, the first step is to choose the data set of prospective detections that is to be searched. The data set should be chosen based on a hypothesis to be tested. We form the hypothesis that electric field oscillations in the auroral plasma are likely to be found during periods having both Pi1B magnetic pulsations, and pulsations in optical emissions. In choosing an event, we also require that PFISR is operating in a raw data collection mode; for otherwise the Nyquist frequency of the temporal sampling is well below the Pc 1 range; the normal temporal sampling for ISR is only a few minutes. However, the ISR is capable of detecting much higher frequency oscillating phenomena, as long as they persist for a sufficiently long time. For example, ISR routinely detects ion acoustic waves. We have identified an observation period that satisfies all these criteria and searched it.

We analyze an 89 s section of PFISR data during which both 0.2 Hz optical pulsations and Pi1B magnetic pulsations were detected, during the recovery phase of a substorm. In order to be easily detected a pulsation (a sine-wave

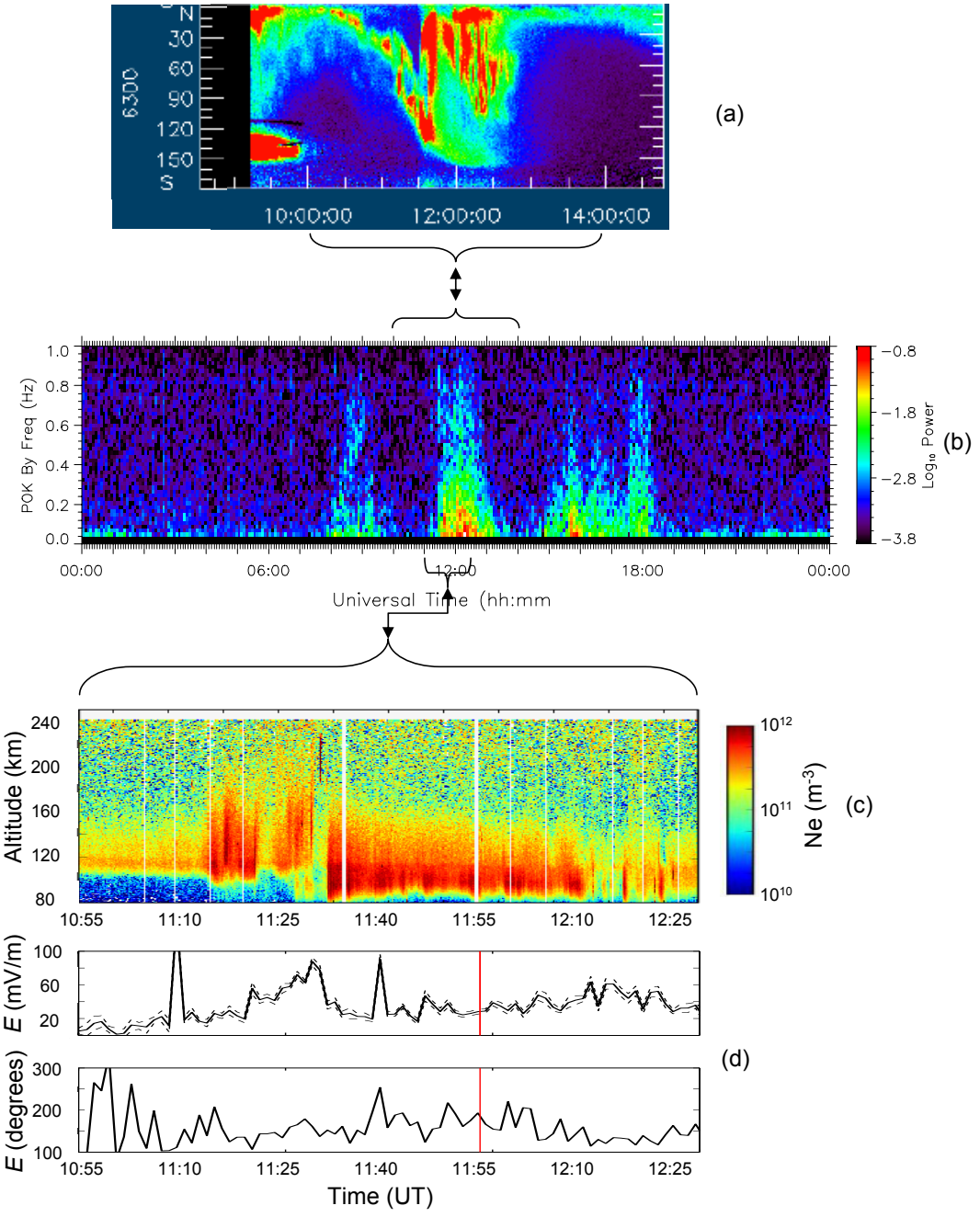

Fig. 1. Geophysical context: **(a)** Keogram from all sky image, **(b)** spectrogram of magnetometer fluctuation, **(c)** altitude/time/density from PFISR, **(d)** electric field from PFISR, with vertical red line showing the time of the pulsations.

oscillation) should either persist for a long time, or it should deeply modulate the back scatter. In performing the analysis we began by searching for pulsations lasting the full 60 s, by analyzing 60 s time series, and searching over altitude. However, this did not yield any statistically significant detections in the frequency range of interest.

Therefore, working on the assumption that the data may still contain shorter lived pulsations, we incrementally reduced the length of the time series analyzed, and performed the search over time and altitude. In doing this we (somewhat arbitrarily) decided to disregard pulsations lasting less than five periods, and thus determined a lower cutoff frequency associated with each time series length. In addition, we fixed an upper search frequency of 2 Hz, partly for statistical reasons described below, and partly based on results from previous magnetometer studies, and IAR theory. In this way

Table 1. PFISR beam labels.

Beam #	azimuth	elevation
1	−85.6°	69.2°
2	121.4°	69.7°
3	−154.3°	81.5°
4	−154.3°	80.5°
5	−154.3°	79.5°
6	−154.3°	78.5°
7 (up $\boldsymbol{B}$)	−154.3°	77.5°

we discovered a 7 s long 1.4 Hz pulsation that appears to be statistically significant.

The method for determining statistical significance is described in detail below. It is based on a statistical test known as the generalized likelihood ratio test (GLRT) (e.g., Kay, 1998), which may be applied in very general circumstances. We apply the GLRT test to the case of detecting a sinusoid in Gaussian white noise, and arrive at a form of periodogram, which is normalized such that the output level can be interpreted in terms of the probability of false alarm, that is, the probability that the output level could be caused by Gaussian white noise. In addition, because of certain non-idealities in our processing, we verify the statistical significance of our results via a Monte Carlo simulation: Gaussian white noise generated by a random number generator is put through the complete processing Algorithm, such that the entire experiment is simulated 1000 times with inputs of pure noise. The conclusion of this exercise is that in the worst case there is a 1 in 67 chance that the detected pulsation is a false alarm, and when the additional evidence is considered (like the apparent presence of the signal in the adjacent beam) the false alarm probability must be taken as much less.

1.2 Geophysical context

Figure 1a shows a keogram from the Poker Flat meridional scanning photometer recorded on 8 March 2009. The keogram shows the phases of a substorm, with growth phase starting at approximately 10:15 UT, and expansion phase onset occurring at 11:30 UT. Recovery phase extends to at least 12:45 UT and shows a proliferation of auroral intensifications near and equatorward of the polar cap boundary.

Figure 1b shows a spectrogram of the magnetic field B_y (which looks more or less identical to the same for B_x) for the same day, from the search-coil magnetometer located at Poker Flat (courtesy of M. Lessard). A classic Pi1B signature is evident that appears to coincide with the expansion phase onset identified in the keogram. Such Pi1B signatures are known to be strongly correlated with expansion phase onset (Lessard et al., 2006).

During this period, the PFISR was operating in a 7 beam mode, with 5 adjacent beams directed up and immediately to the north of magnetic zenith, and 2 outrigger beams for measuring vector electric field in the vicinity of magnetic zenith. The azimuth, elevation, and labeling of the beams is summarized in Table 1.

An altitude-time-intensity plot of electron density from Beam 3, and a plot of the electric field magnitude and direction determined from Beams 1 and 2, are shown in Fig. 1c and d, respectively, for the temporal region immediately surrounding the Pi1B onset. The initiation of auroral plasma deposition, and a ramp up of the electric field, occur simultaneously with the Pi1B onset. The short gap just after 11:30 in the altitude-time-intensity plot corresponds to the period when the aurora is south of Poker flat, as indicated in the keogram of Fig. 1a (Poker Flat is at 90° in Fig. 1a). The two periods of plasma deposition prior to 11:30 appear to be during the equatorward progression of the aurora in the growth phase of the substorm, and prior to the Pi1B signature.

Narrow field optical imagers were also deployed during this period. Figure 2a shows a keogram from the "CLVIS" imager (FOV: 15.5° × 15.5°, 33 Hz, white light), for a 30 s period during the recovery phase of the substorm, when 0.2 Hz pulsations were in evidence. Another imager operating at a lower sampling rate (AVT Guppy camera, FOV: 24.4° × 31.6°, 2 fps, RG645 cutoff-filter) provided a broader temporal context, and showed that the pulsation event did not extend significantly outside of this CLVIS 30 s window. This particular period stands out as the clearest example of pulsations during the substorm.

Both within and to the north of the 0.2 Hz pulsations there also appear faint, quasi-periodic modulations in the range 1.4–2.1 Hz (see Sect. 3.5). These are somewhat clearer to the north of the 0.2 Hz pulsations, perhaps because they are masked by the stronger 0.2 Hz pulsations. Such more rapid modulations of the brightness commonly accompany pulsations (e.g., Sato et al., 2004). This frequency range is at or slightly below the lower limit of what might be termed flickering aurora (e.g., Whiter et al., 2008). To avoid confusion with the nominal frequency range for flickering aurora, we will refer to them as "rapid modulations".

The locations of radar beams 3 through 7 are between the horizontal lines drawn on Fig. 2a. Beams 3 and 4 are north of the 0.2 Hz pulsations, but intersect the more distinct region of rapid modulations. Beams 5 through 7 intersect the 0.2 Hz pulsations.

Figure 2b shows the PFISR backscattered power from Beam 3 for an 89 s period surrounding the pulsations, averaged to 1/4 s resolution in time, and 20 km resolution in range. There appears to be significant temporal structure in the radar data, which is reminiscent of pulsations between one and two Hz. However, due to microscopic rearrangement of electrons within the scattering volume, the backscattered power should be regarded as a random variable; only statistical quantities can be directly related to the macroscopic plasma density. In fact, the standard deviation of

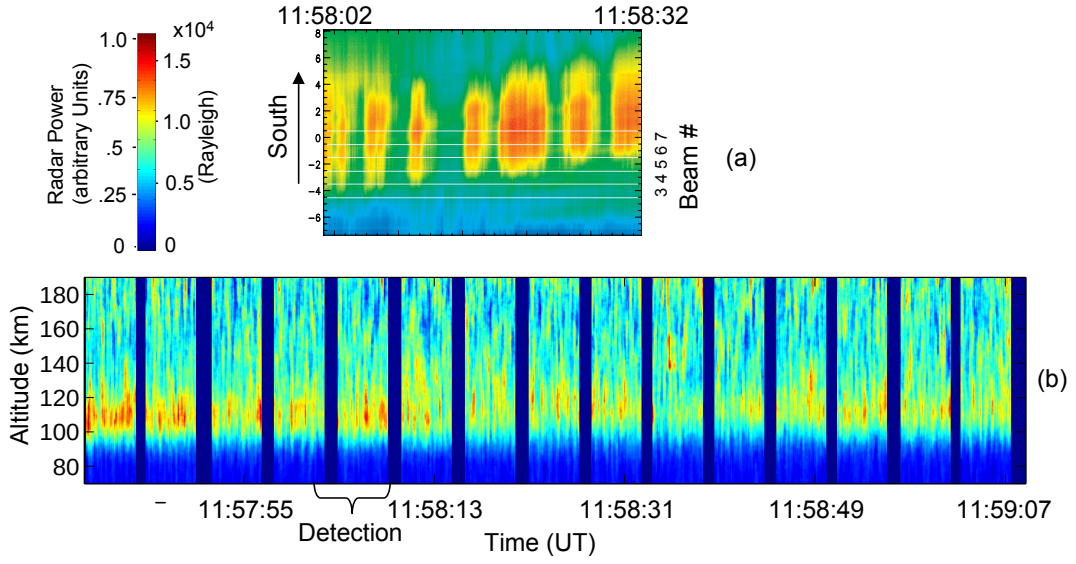

Fig. 2. (a) CLVIS keogram, **(b)** altitude/time/intensity from Beam 3 of PFISR.

the fluctuations seen in Fig. 2b is not significantly above what would be expected from microscopic plasma fluctuations. On the other hand, only by coincidence will microscopic fluctuations take on the form of a sinusoid. Therefore, we may use the likelihood of such a coincidence to establish statistical significance. Section 2 describes basic methodology for doing this, and Sect. 3 describes application of the methodology to the data in Fig. 2a and b.

2 Methodology

2.1 Radar detection

Let $V:\mathbb{N}\to\mathbb{C}$ be a representative time series of the complex voltage received by an ISR, for back scatter from a particular range bin (where $\mathbb{C}$ means the complex numbers and $\mathbb{N}$ means the positive integers). At time $t\in\mathbb{N}$, $V(t)$ can be written

$$V(t)=A\sum_{\alpha=1}^{M(t)}\mathrm{e}^{i\boldsymbol{k}\cdot\boldsymbol{x}_\alpha(t)}, \tag{1}$$

where $\boldsymbol{x}_\alpha(t)$ is the position of the α-th electron at time t, $M(t)$ is the number of electrons in the scattering volume at time t, k is twice the radar wavevector, and A is a constant involving the scattering cross section for an electron, the distance to the scattering volume, and various radar system parameters. The received power (sometimes called the "raw density") can be manipulated

$$\begin{aligned}V(t)V^*(t) &= A^2\sum_{\alpha=1}^{M(t)}\sum_{\beta=1}^{M(t)}\mathrm{e}^{i\boldsymbol{k}\cdot[\boldsymbol{x}_\alpha(t)-\boldsymbol{x}_\beta(t)]}\\ &= A^2\left\{M(t)+\sum_{\alpha\neq\beta}\mathrm{e}^{i\boldsymbol{k}\cdot[\boldsymbol{x}_\alpha(t)-\boldsymbol{x}_\beta(t)]}\right\}\\ &= A^2\left\{M(t)+\sum_{\alpha\neq\beta}\cos\left(\boldsymbol{k}\cdot\left[\boldsymbol{x}_\alpha(t)-\boldsymbol{x}_\beta(t)\right]\right)\right\}\\ &\triangleq A^2M(t)\left\{1+(M(t)-1)\left\langle\cos\left(\boldsymbol{k}\cdot\left[\boldsymbol{x}_\alpha-\boldsymbol{x}_\beta\right]\right)\right\rangle_{\mathcal{F}_t}\right\}\\ &\quad+\delta(t),\end{aligned} \tag{2}$$

where $\langle\cdots\rangle_{\mathcal{F}_t}$ denotes an ensemble average over a collection $\mathcal{F}_t$ of microscopic system configurations that are macroscopically equivalent to the actual microscopic system existing at time t. The notation $\triangleq$ is used to indicate that the time series $\delta:\mathbb{N}\to\mathbb{R}$ is defined by this notion of an ensemble average. Assuming that $\delta(t_i)$ and $\delta(t_j)$ are uncorrelated for $i\neq j$, each real number $\delta(t)$ is a particular realization of the zero-mean random number $\delta_{\mathcal{F}_t}$, where $\delta_{\mathcal{F}_t}$ is defined as randomly chosen from the ensemble $\mathcal{F}_t$. That $\delta_{\mathcal{F}_t}$ is zero-mean follows from the definition $\delta(t)\triangleq V(t)V^*(t)-\langle VV^*\rangle_{\mathcal{F}_t}$, so that $\overline{\delta_{\mathcal{F}_t}}=\langle\delta\rangle_{\mathcal{F}_t}=0$.

In practice, the ensemble average must be approximated as a time average over a finite time interval $\mathcal{I}=\{t_i\,|\,i\in[1,2,\cdots,N]\}$. In this case each $\delta(t)$ is a particular realization of the random number $\delta_{\mathcal{F}_N}$, where $\delta_{\mathcal{F}_N}$ is defined as randomly chosen from the union of the ensembles covering the interval, $\mathcal{F}_N=\bigcup_{i\in\mathcal{I}}\mathcal{F}_{t_i}$. If the statistics are stationary then $\mathcal{F}_{t_i}=\mathcal{F}_{t_j}$ for all i and j, so that $\mathcal{F}_N=\mathcal{F}_t$. More generally, the random number $\delta_{\mathcal{F}_N}$ has mean $\langle\delta\rangle_{\mathcal{F}_N}=\frac{1}{N}\sum_{i=1}^N\langle\delta\rangle_{\mathcal{F}_{t_i}}=0$ and variance $\langle\delta^2\rangle_{\mathcal{F}_N}=\frac{1}{N}\sum_{i=1}^N\langle\delta^2\rangle_{\mathcal{F}_{t_i}}$. With this approximation, the back scattered power over the time interval can be represented as the sum of a deterministic signal plus a zero-mean random number:

$$V(t)V^*(t) = A^2M(t)\left\{1+(M(t)-1)\left\langle\cos\left(\boldsymbol{k}\cdot\left[\boldsymbol{x}_\alpha-\boldsymbol{x}_\beta\right]\right)\right\rangle_{\mathcal{F}_t}\right\} + \delta_{\mathcal{F}_N}. \quad (3)$$

The simple case of Thompson scattering arises when the electrons are randomly distributed over the scattering volume, in which case the $\boldsymbol{k}\cdot\left[\boldsymbol{x}_\alpha(t)-\boldsymbol{x}_\beta(t)\right]$ are uniformly distributed on the interval $[0,2\pi]$, so that $\left\langle\cos\left(\boldsymbol{k}\cdot\left[\boldsymbol{x}_\alpha-\boldsymbol{x}_\beta\right]\right)\right\rangle_{\mathcal{F}_t}=0$. However, because of coulomb repulsion, for a plasma in thermodynamic equilibrium the two-point correlation coefficient $C(\boldsymbol{x}_\alpha-\boldsymbol{x}_\beta)$ for the electron charge density is negative at close range, and zero at long range, so that the ensemble mean $\left\langle\cos\left(\boldsymbol{k}\cdot\left[\boldsymbol{x}_\alpha-\boldsymbol{x}_\beta\right]\right)\right\rangle_{\mathcal{F}_t}$ is negative. This mean has been calculated for a fully-ionized plasma in thermodynamic equilibrium ($T_\mathrm{e}=T_\mathrm{i}$) by Salpeter (1960), with the result

$$M(t)\left\langle\cos\left(\boldsymbol{k}\cdot\left[\boldsymbol{x}_\alpha-\boldsymbol{x}_\beta\right]\right)\right\rangle_{\mathcal{F}_t} = -\alpha^2/(1+2\alpha^2), = -\frac{1}{2}, \text{ if}\alpha\gg1, \quad (4)$$

where $\alpha=1/(kD)$, and D is the Debye length. For a normal ISR $\alpha\gg1$, so that correlations act to reduce the total back scattered power by a factor of one half with respect to the simple case of Thompson scattering.

Regardless, if the total number of particles $M(t)$ in the scattering volume oscillates,

$$M(t) = M_0+\epsilon M_0\cos\omega_0 t, \quad (5)$$

then it is clear that the ensemble mean $A^2M(t)\left\{1+(M(t)-1)\left\langle\cos\left(\boldsymbol{k}\cdot\left[\boldsymbol{x}_\alpha-\boldsymbol{x}_\beta\right]\right)\right\rangle_{\mathcal{F}_t}\right\}$ will oscillate. For example, if the plasma stays in thermodynamic equilibrium, then using Eqs. (4) and (5) in Eq. (3) gives

$$V(t)V^*(t) = A^2\frac{M_0}{2}+A^2\frac{\epsilon M_0}{2}\cos\omega_0 t+\delta_{\mathcal{F}_N} \quad (6)$$

(where $M-1$ was replaced by M). The back scattered power consists of a constant, plus a sinusoid, plus a zero mean random number.

Equation (4) says that the ensemble mean $\left\langle\cos\left(\boldsymbol{k}\cdot\left[\boldsymbol{x}_\alpha-\boldsymbol{x}_\beta\right]\right)\right\rangle_{\mathcal{F}_t}$ is inversely proportional to $M(t)$, and independent of the plasma temperature (over the range of interest), as long as the plasma remains in thermodynamic equilibrium. However, if the plasma is driven out of thermodynamic equilibrium then $M(t)\left\langle\cos\left(\boldsymbol{k}\cdot\left[\boldsymbol{x}_\alpha-\boldsymbol{x}_\beta\right]\right)\right\rangle_{\mathcal{F}_t}$ may change. For example, it is known that the mean back scattered power $A^2M(t)\left\{1+(M(t)-1)\left\langle\cos\left(\boldsymbol{k}\cdot\left[\boldsymbol{x}_\alpha-\boldsymbol{x}_\beta\right]\right)\right\rangle_{\mathcal{F}_t}\right\}$ depends on the electron to ion temperature ratio $\frac{T_\mathrm{e}}{T_\mathrm{i}}$, and this dependence can only come through the term $(M(t)-1)\left\langle\cos\left(\boldsymbol{k}\cdot\left[\boldsymbol{x}_\alpha-\boldsymbol{x}_\beta\right]\right)\right\rangle_{\mathcal{F}_t}$. Therefore, if the plasma is driven by an oscillatory disturbance that modulates $\frac{T_\mathrm{e}}{T_\mathrm{i}}$, then $(M(t)-1)\left\langle\cos\left(\boldsymbol{k}\cdot\left[\boldsymbol{x}_\alpha-\boldsymbol{x}_\beta\right]\right)\right\rangle_{\mathcal{F}_t}$ can be expected to oscillate. Plugging $(M(t)-1)\left\langle\cos\left(\boldsymbol{k}\cdot\left[\boldsymbol{x}_\alpha-\boldsymbol{x}_\beta\right]\right)\right\rangle_{\mathcal{F}_t} = -1/2(1-\epsilon\cos\omega_0 t)$ into Eq. (3) again gives Eq. (6), that is, sinusoidal modulation of $\frac{T_\mathrm{e}}{T_\mathrm{i}}$ also leads to back scattered power consisting of a constant, plus a sinusoid, plus a zero mean random number.

It is possible that both M and $\frac{T_\mathrm{e}}{T_\mathrm{i}}$ are sinusoidally modulated. In this case the ensemble mean back scattered power $A^2M(t)\left\{1+(M(t)-1)\left\langle\cos\left(\boldsymbol{k}\cdot\left[\boldsymbol{x}_\alpha-\boldsymbol{x}_\beta\right]\right)\right\rangle_{\mathcal{F}_t}\right\}$ will contain the sinusoidal modulation along with harmonics.

2.2 Signal to noise ratio

In Sect. 2.1 we argued that sinusoidal modulation of either the number of electrons in the scattering volume M, or the temperature ratio $\frac{T_\mathrm{e}}{T_\mathrm{i}}$, results in back scattered power consisting of a constant, plus a sinusoid, plus a zero mean random number in the form of Eq. (6).

Consider N complex voltage samples $V(t_i)$ taken once per pulse of the radar, for a particular range bin. It is well known that the decorrelation time for a thermal plasma is much less than any practical inter pulse period (e.g., Farley, 1972). Therefore, $\delta(t_i)$ and $\delta(t_{j\neq i})$ are uncorrelated. It is also well known that V is well described by a zero-mean Gaussian pdf

$$f(V) = \frac{1}{2\pi\sigma^2}\exp\left(\frac{-|V|^2}{2\sigma^2}\right). \quad (7)$$

Therefore, the pdf for $y=|VV^*|$ is a Chi-Squared distribution of order 2:

$$f(y) = \frac{1}{2\sigma^2}\exp\left(\frac{-y}{2\sigma^2}\right). \quad (8)$$

The mean and variance over the pdf (8) are $A^2M_0/2$ and $\mathrm{Var}(\delta(t_i))$, respectively (from Eq. 6, where we drop the subscript on δ). Therefore, they are computed as

$$A^2\frac{M_0}{2} = 2\sigma^2 \quad \text{and} \quad \mathrm{Var}(\delta(t_i)) = 4\sigma^4. \quad (9)$$

The discrete form of the Wiener-Khintchine theorem gives

$$N\mathrm{Var}(\delta(t_i)) \cong \sum_{i=1}^{N}\delta^2(t_i) = \frac{1}{N}\sum_{i=1}^{N}|\Delta(\omega_i)|^2, \quad (10)$$

where Δ is the discrete Fourier transform (DFT) of δ, and N is the number of samples. We have argued that the spectrum of $\delta(t_i)$ is white (i.e., $\delta(t_i)$ and $\delta(t_{j\neq i})$ are uncorrelated). To obtain the level of this white spectrum set $\Delta(\omega_i)$ to a constant, which gives

$$|\Delta(\omega_i)|^2 = N4\sigma^4, \quad (11)$$

by using Eqs. (9) and (10). The DFT of $\cos\omega_0 t$ has peaks with level $\frac{N}{2}$. Therefore, incorporating the factor ϵ from Eq. (6), and using Eqs. (9) and (11), we obtain the signal to

noise ratio for detection of a sinusoidal modulation of plasma density in pure plasma back scatter (SNR_p) as

$$SNR_p = \frac{\left(A^2 \frac{\epsilon M_0}{2} \frac{N}{2}\right)^2}{|\Delta(\omega_i)|^2} = \frac{\left(\sigma^2 \epsilon N\right)^2}{N 4\sigma^4} = \frac{\epsilon^2 N}{4}. \quad (12)$$

This result assumes that there is no additive noise, that is, that the noise arises entirely from plasma fluctuations. This is realistic for high plasma density, but for moderate plasma density an additive noise level should be added to the denominator of Eq. (12), to yield the true signal to noise ratio (SNR).

2.3 Statistical significance

The problem for this work is to analyze the time series $|u|^2(t_i)$, which is assumed to have the form (6), and assign a probability to the postulate that ϵ is zero. We will refer to this as the probability of false alarm (P_{FA}), since it is the probability that it would be a mistake to conclude that $\epsilon \neq 0$, that is, it is the probability that the time series might be the result of a pure noise input. This is a classical problem in statistical detection that conforms to what is known as the linear model: the data have the form $\boldsymbol{x} = \mathbf{H}\boldsymbol{\epsilon} + \boldsymbol{w}$, where $\boldsymbol{x}$ is an $N \times 1$ data vector, $\boldsymbol{\epsilon}$ is a $p \times 1$ vector of signal-strength parameters, $\mathbf{H}$ is an $N \times p$ known "observation matrix" (which determines the functional form of the signal, sinusoidal in our case), and $\boldsymbol{w}$ is a random Gaussian vector with zero mean and standard deviation σ. Therefore, we can apply the theorems of statistical detection theory.

The Neyman Pearson theorem (e.g., Kay, 1998) states that the statistically optimal detector decides $\epsilon \neq 0$ if

$$\frac{p(\boldsymbol{x}|\boldsymbol{\epsilon} \neq 0)}{p(\boldsymbol{x}|\boldsymbol{\epsilon} = 0)} > \gamma, \quad (13)$$

where $p(\boldsymbol{x}|\boldsymbol{\epsilon} \neq 0)$ is the probability of finding the data $\boldsymbol{x}$ if $\boldsymbol{\epsilon} \neq 0$, $p(\boldsymbol{x}|\boldsymbol{\epsilon} = 0)$ is the probability of finding the data $\boldsymbol{x}$ if $\boldsymbol{\epsilon} = 0$, and the choice of γ sets the acceptable false alarm rate. The test given in Eq. (13) is known as the likelihood ratio test. Its application requires knowledge of the conditional probabilities $p(\boldsymbol{x}|\boldsymbol{\epsilon} \neq 0)$ and $p(\boldsymbol{x}|\boldsymbol{\epsilon} = 0)$, which, in our case, requires knowledge of the noise level, and knowledge of the actual non-zero value that the signal-strength ϵ will attain (if it is non-zero). Hence, the likelihood ratio test cannot be directly applied to our problem.

However, in the event that there are unknown parameters, the generalized likelihood ratio test (GLRT) is recommended, for example by Kay (1998), as being proven in practical applications, and as retaining certain optimal properties. The GLRT consists of finding the maximum likelihood estimates (MLEs) of the unknown parameters, and employing them to form the likelihood ratio. Theorem 9.1 from *Kay* [1998] determines the precise form of the GLRT for the classical linear model. We have applied this general theorem to the problem of detecting a sinusoidal signal of unknown amplitude and phase, in white Gaussian noise of unknown variance. The result, found in the Appendix, is the detector

$$T_\omega(\boldsymbol{x}) = \frac{N-2}{2} \frac{\left[\sum_{n=1}^N \sin(\omega t_n - \alpha) x_n\right]^2 / \Gamma + \left[\sum_{n=1}^N \cos(\omega t_n - \alpha) x_n\right]^2 / (N - \Gamma)}{\sum_{n=1}^N x_n^2 - \left[\sum_{n=1}^N \sin(\omega t_n - \alpha) x_n\right]^2 / \Gamma - \left[\sum_{n=1}^N \cos(\omega t_n - \alpha) x_n\right]^2 / (N - \Gamma)} > \gamma, \text{ where}$$

$$\alpha = \frac{1}{2} \arctan\left(\frac{\sum_{n=1}^N \sin 2\omega t_n}{\sum_{n=1}^N \cos 2\omega t_n}\right), \text{ and}$$

$$\Gamma = \sum_{n=1}^N \sin^2(\omega t_n - \alpha). \quad (14)$$

The GLRT detector (14) is a form of normalized periodogram, which may be compared to the well known Lomb-Scargle normalized periodogram. Like the Lomb-Scargle normalized periodogram, the GLRT is a constant false alarm rate (CFAR) detector, which means that the threshold γ uniquely determines the probability of false alarm, independent of other parameters such as the unknown noise level, and the unknown signal level. The difference between the two periodograms lies in the estimation of the unknown noise variance, which takes a more sophisticated form in the GLRT. Specifically, as seen in the denominator of $T_\omega(\boldsymbol{x})$, estimation of the noise variance for the GLRT involves compensation for the possible presence of a signal. This makes the GLRT more sensitive to weak signals, which is why we choose to employ it here. Also, a byproduct of the GLRT is an estimate of the amplitude and phase of any detected signal.

Actually, the noise $\boldsymbol{w}$ contained in the last term of Eq. (6) is white, but not Gaussian. However, by averaging over a sufficiently large number n of pulses, so that $|u|^2(t_i)$ is downsampled to $|u|^2(nt_{\frac{i}{n}})$, the central limit theorem provides that the noise acquires a Gaussian distribution. Because this averaging process is a lowpass filter operation, it does not affect the signal to noise ratio (12). It does, however, affect the Nyquist frequency of the sampling. This is the reason we have chosen to limit our search to frequencies less than 2 Hz. This limitation is a matter of convenience, and is not strictly required.

The exact detection performance (holds for finite data records) is given by

$$P_{FA} = \int_\gamma^\infty \mathrm{d}y \, F_{2,N-2}(y) \equiv Q_{F_{2,N-2}}(\gamma), \quad (15)$$

where F_{ν_1,ν_2} denotes the central F distribution with ν_1 numerator degrees of freedom, and ν_2 denominator degrees of freedom. Equation (15) gives the probability of false alarm for investigation of a single fixed frequency ω. If we search over a range of M independent frequencies (independent, as determined by the time sampling), then the probability of

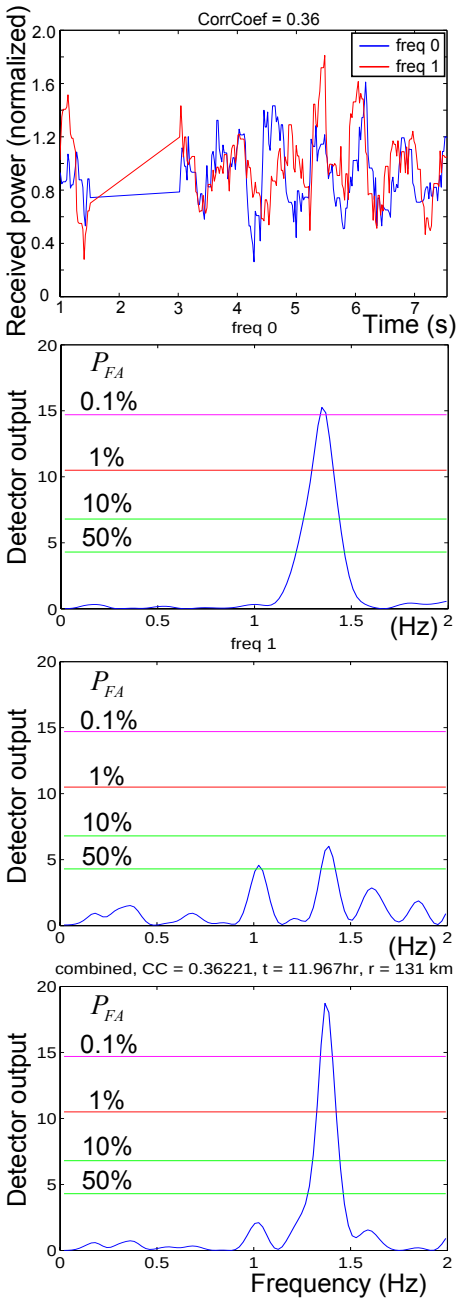

Fig. 3. Beam 3 weighted time series and detector output for the two radar frequencies, and for the combined time series.

false alarm is worked out as follows:

$$
\begin{aligned}
P_{\mathrm{FA}} &= \Pr\left\{\exists i, T_{\omega_i}(\boldsymbol{x}) > \gamma \,|\, \boldsymbol{\epsilon} = 0\right\} \\
&= 1 - \Pr\left\{\forall i, T_{\omega_i}(\boldsymbol{x}) < \gamma \,|\, \boldsymbol{\epsilon} = 0\right\} \\
&= 1 - \prod_i \Pr\left\{T_{\omega_i}(\boldsymbol{x}) < \gamma \,|\, \boldsymbol{\epsilon} = 0\right\} \\
&= 1 - \prod_i \left(1 - \Pr\left\{T_{\omega_i}(\boldsymbol{x}) > \gamma \,|\, \boldsymbol{\epsilon} = 0\right\}\right) \\
&= 1 - \left(1 - Q_{F_{2,N-2}}(\gamma)\right)^M, \qquad (16)
\end{aligned}
$$

where the notation Pr denotes "probability," $\exists$ denotes "there exists", and $\forall$ denotes "for all". The integral (15) can be evaluated numerically.

3 Data analysis

3.1 Analysis of a single radar frequency, and details of processing

The detector (14) has been to applied the radar data shown in Fig. 2a, between altitudes of 90 km and 160 km. The detector (14) was applied to weighted averages of 7 s time series taken over 20 km in altitude, where the weighting was by the inverse standard deviation of each time series. Thus, each point in the image of Fig. 2b was assigned a detector output level for each independent frequency, determined from the 7 s and 20 km surrounding it. When plotted versus frequency the output levels at each point form a periodogram.

In addition, the radar transmitted pulses at two different transmit frequencies (labeled 0 and 1) within each 21 ms inter pulse period (IPP), which were diplexed and sampled separately. The difference between the transmit frequencies was chosen to ensure statistical independence of the samples, the criteria for which can be found in (Farley, 1972; Sulzer, 1986). The two resulting time series were put through the detector separately, as well as being averaged together (with weighting by the inverse standard deviation) and the result put through the detector. Thus, to each point in time and altitude there are assigned two independent periodograms computed from two independent time series, and a third computed from the coherent combination of the two independent time series. The three periodograms comprising the most statistically significant detection from the 89 s data set are shown in Fig. 3, along with the two associated independent time series. This most statistically significant detection was found in beam 3, at an altitude of 131 km, during the first 7 s of the pulsations seen in the optical image of Fig. 2.

Before application of the detector (14) the raw data recorded by PFISR was passed through an outlier removal and temporal averaging algorithm, so as to produce Gaussian statistics as required to achieve the theoretical performance of the detector (as discussed in Sect. 2.3). Each point in the raw data was assigned the 1/4 s temporal window surrounding it, and the sample median of the squared-complex-modulus (median of $|u|^2$) determined. This median was used to estimate the Chi-Squared distribution (8), an estimate that should be robust to the presence of outliers. The estimated distribution was then used to compute the level such that there is a 50% chance that the modulus-squared of at least one point in the 1/4 s time series will exceed it. Any points above this level were taken to be outliers. The modulus-squared of the remaining points were averaged and the result assigned to the central point. The IPP for each beam

was 21 ms, so that the 1/4 s periods contained 12 points each. The image shown in Fig. 2b also has an overall noise level subtracted (subsequent to the outlier removal), and a range-squared scaling factor applied. The overall noise level was subtracted before the formation of the weighted altitude averages described above, so that the time series shown in Fig. 3 (and Fig. 6 to be described later) also have the noise removed.

In deriving (14), we did not require that the time samples t_n be evenly spaced, and in fact the time series shown in Fig. 3 has a gap in it. When sine waves are sampled with this time series, containing a gap, the resulting vectors are not exactly orthogonal. This allows the possibility that there could be a false response at a given frequency due to "leakage" from other frequencies that do not have orthogonal samplings. This does not mean that the equation for detection performance (15) is invalid; it follows from theorem 9.1 of Kay (1998), and therefore must be valid to the extent that the hypothesis testing problem is as assumed. However, the hypothesis was that there was either white noise, or white noise plus a single sinusoid; leakage from a strong signal at another frequency was not contemplated.

Equation (16) gives the probability that at least one of M independent frequencies will exceed the level γ, and there remains the problem of determining what frequencies are independent. For the DFT, the response at different frequencies is independent because the evenly spaced samples of sine waves that form the basis vectors are orthogonal. Although this orthogonality does not hold exactly for the time sampling of the postulated detection seen in Fig. 3, it may hold in an approximate sense. To test this we plot in Fig. 4a and b the decibel response of the detector (14), with $\omega = 2\pi\,1.4$ Hz, to sinusoidal x with frequency ranging from 0 to 25 Hz, for the exact time sampling of the postulated detection. The first side lobe is 40 dB down, and it is evident that there is no significant leakage from distant frequencies. Therefore, the non-orthogonality does not significantly affect the detector for 1.4 Hz signals. However, Fig. 4c shows the similar plot around the frequency 0.2 Hz, and shows that for this center frequency the detector does have a side lobe at 0.1 Hz that is less than 20 dB down. For this and other reasons we will use this detector only above 0.5 Hz.

The relevant question, for application of Eq. (16), is how many independent frequencies are in the band of interest? Here we refer to the results of Horne and Baliunas (1986), who find that for almost any time sampling the number of independent frequencies between zero and the Nyquist frequency is approximately the number (N) of independent points in the time series. Armed with this number we can apply Eq. (16).

By averaging to 1/4 s we have reduced the number of independent points to $\frac{7}{0.25} = 28$, and the Nyquist frequency to $\frac{1}{(2\times 0.25)} = 2$ Hz. Applying Eq. (16) with these numbers gives the four significance levels plotted in the periodograms of Fig. 3. To obtain the correct output levels from Eq. (14), it was necessary to account for the oversampling, which required rescaling the MLE estimate of the variance by the oversampling factor of 12. (A Monte Carlo simulation was done to verify the correctness of the method.) The lowest significance level (green) corresponds to 50% P_{FA}, the next (also green) to 10% P_{FA}, the next (red) to 1% P_{FA}, and the highest (magenta) to 0.1% P_{FA}. It is evident from examining the periodogram for frequency 0 in Fig. 3 that we have a likely detection. The P_{FA} at the periodogram peak is one in one thousand ($P_{\mathrm{FA}} = 0.1\%$). However, we must keep in mind that in scanning the data shown in Fig. 2b we have searched quite a few independent time series, and thereby increased the odds of a false alarm.

3.2 Analysis of two radar frequencies

As noted in Sect. 3.1, the time series produced by the two transmit frequencies are statistically independent. This means that if the plasma density is constant, the correlation-coefficient between the two time series will approach zero (as the length of the series increases, or in an ensemble-average sense); in this case the variability in each time series is caused by additive noise and microscopic rearrangement of the electrons in the plasma (i.e., at the scale of the radar wavelength), neither of which interest us here. By contrast, a statistically significant positive correlation-coefficient between the two time series is an indicator that the radar is detecting a (macroscopic) plasma density modulation. The significance of a correlation coefficient can be determined by the p-value, which is the probability of getting a correlation as large as the observed value by random chance, when the true correlation is zero. Therefore, as an initial screening factor, we have determined to require that any postulated detection in a 7 s series has correlation coefficient greater than 0.2. The top panel in Fig. 3 shows the time series produced by frequencies 0 and 1 for the postulated detection – the correlation coefficient is 0.36. Visual examination of the overlayed time series compels one to believe that the two independent transmit frequencies are responding to the same macroscopic plasma density modulation.

But is the modulation a sinusoidal one? The periodograms produced from the two independent transmit frequencies are necessarily independent, so that the appearance of a peak at the same frequency in both periodograms is a strong indicator that the plasma contains a sinusoidal fluctuation at that frequency. Specifically, the probability of false alarm for deciding $\epsilon \neq 0$ from peaks of magnitude a_1 and a_2, at the same frequency, in the two independent periodograms, is computed as

$$\begin{aligned} P_{\mathrm{FA}} &= \Pr\left\{\exists i, \left(T_{\omega_i}(x_1) > a_1 \wedge T_{\omega_i}(x_2) > a_2\right) | \epsilon = 0\right\} \\ &= 1 - \Pr\left\{\forall i, \sim \left(T_{\omega_i}(x_1) > a_1 \wedge T_{\omega_i}(x_2) > a_2\right) | \epsilon = 0\right\} \\ &= 1 - \prod_i \Pr\left\{\sim \left(T_{\omega_i}(x_1) > a_1 \wedge T_{\omega_i}(x_2) > a_2\right) | \epsilon = 0\right\} \end{aligned}$$

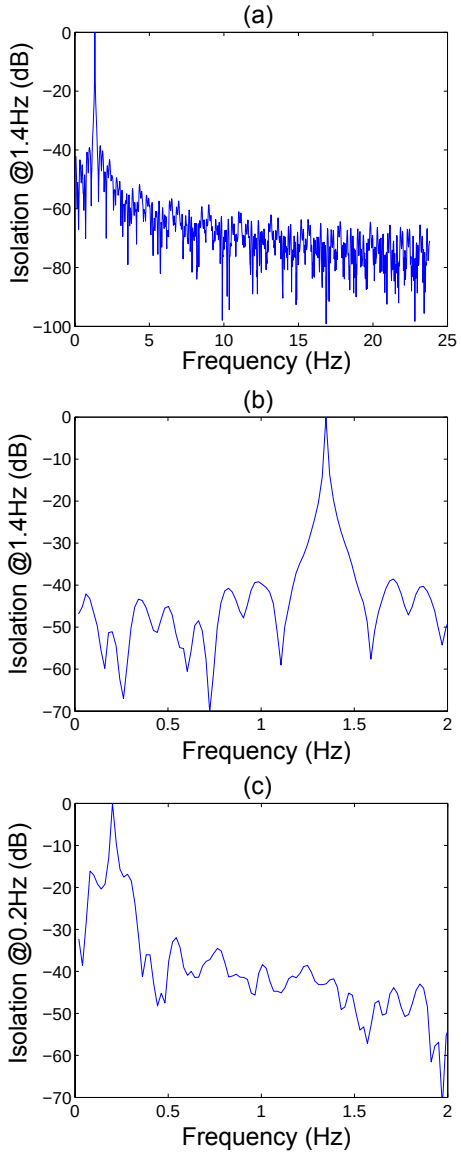

Fig. 4. Detector isolation: **(a)** around 1.4 Hz center frequency to 25 Hz; **(b)** around 1.4 Hz center frequency to 2 Hz; and **(c)** around 0.2 Hz center frequency to 2 Hz.

$$= 1 - \prod_i \left[1 - \Pr\left\{T_{\omega_i}(x_1) > a_1 \wedge T_{\omega_i}(x_2) > a_2 | \epsilon = 0\right\}\right]$$

$$= 1 - \left[1 - Q_{F_{2,N-2}}(a_1) Q_{F_{2,N-2}}(a_2)\right]^M, \quad (17)$$

where $\wedge$ denotes "and", and $\sim$ denotes "not". Applying Eq. (17) to the periodograms for frequency 0 and frequency 1 in Fig. 3 gives $P_{\mathrm{FA}} = 0.0005\%$, or 5 in 1 000 000.

This result applies in the case that a decision (regarding $\epsilon \neq 0$) is made without knowledge of the phase relationship between the time series for the two different transmit frequencies. To factor in the odds of the additional occurrence that the two independent time series appear to be in phase (concluded by visual examination of Fig. 3), multiply P_{FA} by the odds of this under the condition $\epsilon = 0$, which are roughly $\frac{36°}{180°} = 0.2$. This reduces P_{FA} to 1 in 1 000 000.

However, this result applies in the case that we tested only the time series associated with one altitude and time. In point of fact, for each of 5 radar beams in the optical field, we looked at all altitudes and times within an 89 s × 50 km time/altitude interval, sampled in steps of 1 s and 3/4 km – roughly $89 \times \left(\frac{50}{0.75}\right) = 5933$ altitude/time pairs. The time series for each altitude/time pair are drawn from a data set with 1/4 s time resolution, and 20 km altitude resolution. How many independent time series have we looked at? Were it not for the oversampling the answer would be merely $5 \times \frac{89}{7} \times \frac{50}{20} = 159$, which would increase P_{FA} to 1 in 6000. However, the oversampling will further increase P_{FA}, and it is difficult to say by how much. Therefore, we will take 1 in 6000 as the lower bound on P_{FA}, and consider in Sect. 3.3 a more conservative Monte Carlo approach to estimating P_{FA}.

3.3 Monte Carlo simulation

As a more conservative approach to assessing the probability that the detection of Fig. 3 might be a false alarm, we have applied the brute force approach of replacing the radar data collected from a single beam of the radar over the 89 s × 50 km time/altitude interval with numbers generated by a random number generator, 1000 times (without reseeding the generator). The synthetic data are sampled using the same time sampling, with gap, used for the actual data. Thus there are 1000 dual-frequency, single-beam, synthetic experiments to compare with the actual dual-frequency, 7-beam, live experiment (including the two outlier beams). The comparison was established by defining a real number valued metric, so that each experiment was assigned three P_{FA}s, one each for the frequency ranges 0.5–1.0 Hz, 1.0–1.5 Hz, and 1.5–2.0 Hz.

The data for the synthetic experiments was generated as random numbers taken from the same statistical distribution that characterizes ISR back scatter from a constant uniform high density plasma. Specifically, the synthetic data is generated as complex numbers v taken from the Gaussian statistical distribution 7. The choice of the standard deviation σ is of no consequence, as the GLRT detector is a CFAR detector, i.e., σ is normalized away (this has been verified by direct test).

The P_{FA} metric was defined to be the minimum value, taken over all the altitude/time pairs (described in the last paragraph of Sect. 3.2), and over the chosen frequency range, of the product of the three P_{FA}s generated by the GLRT detector applied to the two independent time series derived from the two transmit frequencies, and to the mean of these two time series, evaluated at the same particular frequency. In addition, the correlation coefficient between the two independent time series is used as a screening factor: only altitude/time pairs with correlation coefficient greater than 0.2

are included. As previously described, the two independent time series for the postulated detection are shown in the top panel of Fig. 3, and the three GLRT outputs are plotted versus frequency in the bottom three panels. Graphically, the metric can be visualized from these bottom three panels: Three P_{FA} values are computed from the three detector output values intersected by a vertical line through the three panels, drawn at a particular frequency, and then these three values are multiplied together; the minimum of the resultant, taken over a chosen frequency range, is then stored with reference to this particular altitude and time (i.e., the time at the center of the 7 s series). The minimum of these stored values, taken over all altitudes and times in the experiment, is the P_{FA} metric for the experiment, for the chosen frequency range.

The P_{FA} metric is chosen to capture, as much as is possible, all the relevant detection criteria in a single number. The reasons for using the product of the P_{FA}s from the two independent transmit frequencies were described in Sect. 3.2. The mean of the two time series is not, of course, an independent time series. However, the extent to which a sinusoidal signal detected in both of the two independent time series, is also present in the mean time series, is a measure of the extent to which the two apparent signals had the same phase. Hence, by taking the product with the P_{FA} from the mean time series we are factoring in independent information regarding whether a macroscopic plasma density modulation is responsible. As described in Sect. 3.2, screening by the correlation coefficient gives a similar assurance.

The green, red, and yellow histograms in Fig. 5 contain the natural logs of the P_{FA} metrics for the 1000 synthetic experiments, in the frequency ranges 0.5–1.0 Hz, 1.0–1.5 Hz, and 1.5–2.0 Hz, respectively. Panels (a), (b), and (c) of Fig. 5 overlay blue bars depicting the 7 P_{FA} metric values (natural logs thereof) for the 7 beams of the live experiment, for the frequency ranges 0.5–1.0 Hz, 1.0–1.5 Hz, and 1.5–2.0 Hz, respectively. Visual inspection reveals that for the frequency range 1.0–1.5 Hz (red histogram in panel b), one beam (beam 3) of the live experiment presents as an outlier.

To quantify this result the cumulative distribution function (CDF) of the P_{FA} metric is estimated from the quantiles taken over the 1000 synthetic experiments, for the frequency range 1.0–1.5 Hz. (The fractional position of each data point in the ordered data set is an estimate of the CDF evaluated at the value of the data point.) The natural log of the estimated CDF is plotted versus the natural log of the P_{FA} metric in panel (d) of Fig. 5. The vertical line shows the position of the apparent outlier from beam 3 of the live experiment. The smoothness of the curve suggests that a good estimate of the CDF has been established.

The P_{FA} metric is not a complete or perfect measure of all the criteria that went into choosing the response shown in Fig. 3 as a candidate detection. In examining the points in the tails of the distributions shown in Fig. 5, it is found that some of them would have been discarded because they in fact represented a very strong response in only one (synthetic)

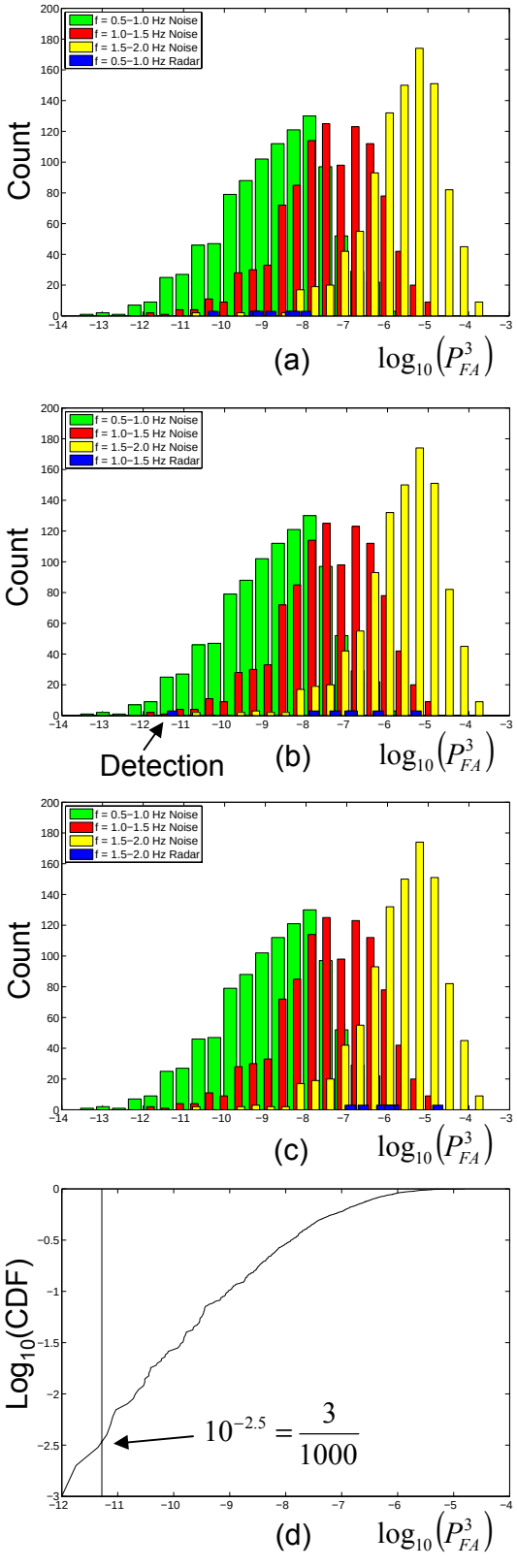

Fig. 5. Histograms of noise for three frequency ranges, with data points for the 5 beams in blue, along with the CDF for panel (b): **(a)** 0.5–1.0 Hz, **(b)** 1.0–1.5 Hz, **(c)** 0.5–1.0 Hz, **(d)** CDF with vertical line indicating the detection.

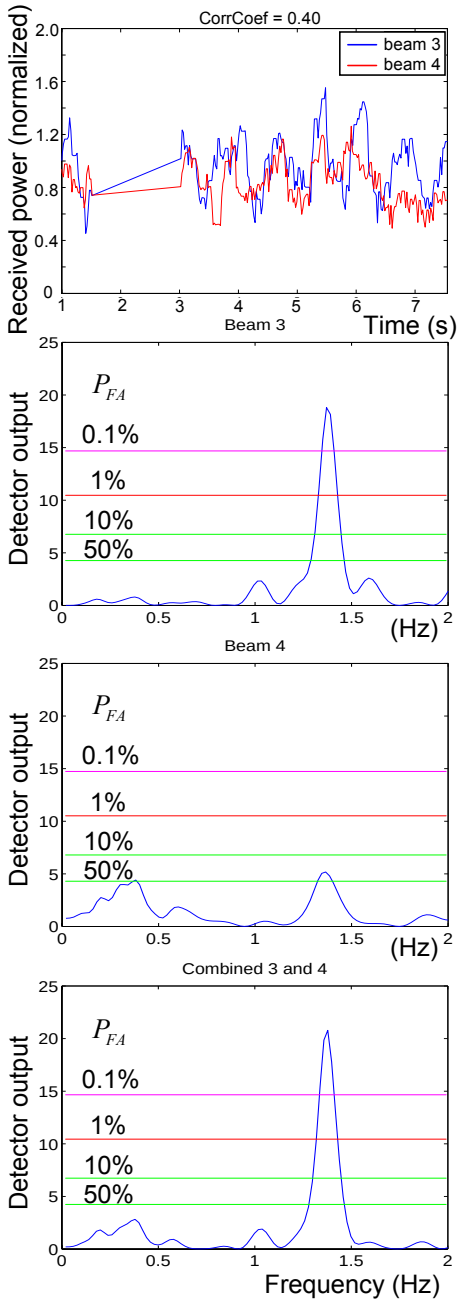

Fig. 6. Weighted time series and detector output for beams 3 and 4, and for the combined time series.

transmit frequency, with no response in the other. Had we encountered such an example in the actual data we would have concluded that although it was very unlikely to have been caused by Gaussian white noise, it was also very unlikely to be caused by a macroscopic plasma density modulation, and hence that it is most likely caused by an unmodeled noise source – such are the limitations of these statistical treatments. For this reason, we believe that the low P_{FA} tails in the histograms are somewhat enhanced, and that the result of this Monte Carlo analysis may be somewhat pessimistic.

The conclusion shown in Fig. 5d is that there is a 3 in 1000 chance, per beam, of producing a false response like that shown in Fig. 3. However, we would have been equally happy to find the response in any of the 5 beams located in the optical field. Therefore, we conclude from the Monte Carlo analysis that the postulated detection shown in Fig. 3 has a 1 in 67 chance of being a false alarm. However, because of the likely artificial enhancement of the low P_{FA} tail described in the previous paragraph, we regard this as an upper bound.

3.4 Analysis of two beam positions

Beyond the results of Sects. 3.1 through 3.3, there is an additional piece of information which might be regarded as clinching the case for detection of a 1.4 Hz pulsation. The top panel of Fig. 6 shows the mean time series (mean over the two transmit frequencies) for beam 4 overlayed with the same for beam 3, for the altitude/time pair of Fig. 3. The correlation coefficient between the two is 0.4. Visual examination leaves little doubt that the two beams contain the same oscillating sinusoidal signal.

The GLRT periodogram for beam 4 is shown in the third panel of Fig. 6. Although much weaker than the response for beam 3 (seen either in the second panel of Fig. 6, or in the fourth panel of Fig. 3), there is a definite response at the same frequency. When the GLRT is applied to the mean of the beam 3 and beam 4 time series (i.e., the two in the top panel of Fig. 6), the result is stronger than either of the two individual responses (the strongest response presented herein), which gives quantification to the strong visual suggestion that the same sinusoidal signal is present in both beams.

As indicated in Table 1, beams 3 through 7 are spread from north to south in one degree increments, and the beam width is also about one degree, so that they are essentially adjacent. Because beam 4 is the closest to beam 3, the result is consistent with a physical cause. There was no hint of a related signal in any of the other, more distant beams, which helps to dissuade any doubt of a systematic cause. When the fact that the same sinusoidal signal is seen in the adjacent beam 4 is added to the evidence presented in Sects. 3.1 through 3.3 for a signal in beam 3, it seems clear that the radar has detected a macroscopic sinusoidal plasma density modulation at a frequency of 1.4 Hz, in the radar frame.

3.5 Analysis of rapid modulations in CLVIS image

The detector (14) has also been applied to the CLVIS keogram at the positions of beams 3 and 4, and the results shown in Fig. 7. Figure 7a and b shows the detector output and time series, respectively, at the location of beam 3, for 5 s of data beginning 2 s before the end of the period of the radar detection. A peak is evident at 1.4 Hz with P_{FA} less than 1 in 100. This matches the frequency of the radar detection. The time series also shows large low frequency fluctuations.

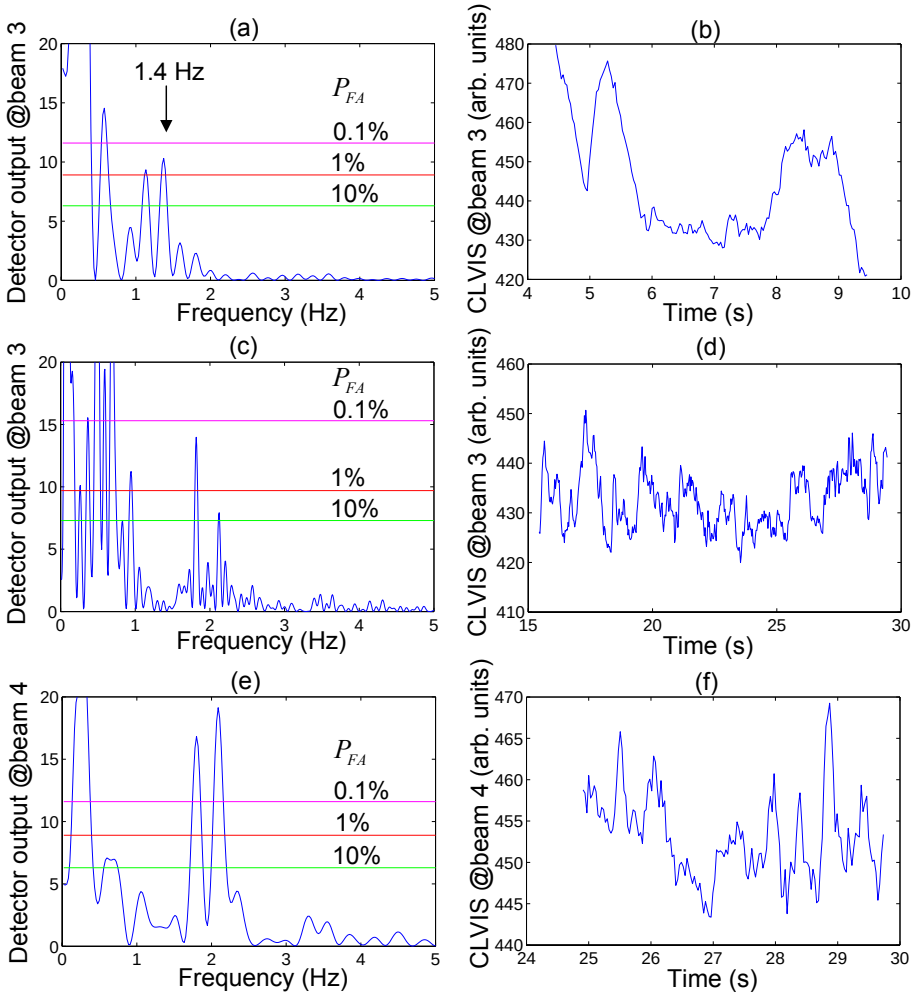

Fig. 7. GLRT detector applied to the CLVIS keogram at the locations of beams 3 and 4. **(a)** and **(b)** Detector output and time series at beam 3, for 5 s beginning 11:58:06. **(c)** and **(d)** Detector output and time series at beam 3, for 14 s beginning 11:58:17. **(e)** and **(f)** Detector output and time series at beam 4, for 5 s beginning 11:58:27. The time axes show the seconds after 11:58:03.

If the five second period analyzed is placed earlier, so that it begins commensurate with the period of the radar detection, then the low frequency fluctuations are stronger, and the peak at 1.4 Hz is not significant. The large low frequency fluctuations mean that the assumptions for the hypothesis testing problem are not satisfied, and the P_{FA} levels indicated are artificially high. It is possible that the low frequency fluctuations are masking the 1.4 Hz peak. However, good judgment requires that we regard the 1.4 Hz peak as tantalizing, but not conclusive.

Figure 7c and d shows the detector output and time series, respectively, at the location of beam 3, for 14 s of data beginning 9 s after the period of the radar detection. Two peaks are evident, one at 1.8 Hz and one at 2.1 Hz. The P_{FA} for the former is significantly less than 1 in 100. There are also some lower frequency fluctuations. However, the peak at 1.8 Hz appears more clearly distinct than the 1.4 Hz peak in Fig. 7a. In addition, the fact that the 1.8 Hz peak is strong over a 14 s interval (as opposed to a 5 s interval) leads us to conclude that it is more likely to represent an actual signal in the data.

Figure 7c and d shows the detector output and time series, respectively, at the location of beam 4, for 5 s of data beginning 18 s after the period of the radar detection. Two peaks are evident, one at 1.8 Hz and one at 2.1 Hz. The P_{FA} for both peaks is significantly less than 1 in 1000. In this case the low frequency fluctuations are much less apparent than in any of the above cases, and the peaks are very convincing. The sinusoidal signal is evident to the naked eye. These peaks match the frequencies of the two peaks seen earlier in beam 3. Although the beam 3 period overlaps the beam 4 period, the beam 3 data retains a clear peak if it is truncated to remove the overlap.

Combining these results, we conclude that the temporal neighbourhood (within 10 to 15 s) of the radar detection contains 1.8 Hz modulations of the auroral particle precipitation. During the actual 7 s period of the radar detection there is

evidence, although not conclusive, of a 1.4 Hz oscillation (matching the frequency of the radar detection). The period of the radar detection also exhibits large low frequency fluctuations that are not seen in the radar data, and which might mask a 1.4 Hz oscillation. However, we note that there is no radar detection associated with what appear to be stronger 1.8 Hz modulations, later in the time interval; there is not a one-to-one correspondence between the radar and optical detections.

4 Discussion

4.1 Plasma reference frame

If the 1.4 Hz oscillating signal observed in the radar frame is related to Alfvén waves propagating in the plasma, then the natural reference frame is the one drifting with the plasma $\boldsymbol{E}\times\boldsymbol{B}$ velocity. In the case of Alfvén-wave-produced precipitation or electric fields, there should be a density or temperature wave propagating in the direction perpendicular to $\boldsymbol{B}$ (or a sum of such waves), which may have a relatively short wavelength. There may be a significant Doppler shift contribution to the frequency observed in the radar frame. Therefore, interpretation of the measurement results will be aided if we put some constraints on the Doppler shift associated with the conversion from the the radar-fixed frame to the $\boldsymbol{E}\times\boldsymbol{B}$ frame.

The radar beam width is about 1°, which makes for a resolution of about 1 km in the zonal direction (which is the direction of the $\boldsymbol{E}\times\boldsymbol{B}$ drift, as seen in Fig. 1). We are well assured, therefore, that if the 1.4 Hz oscillation is associated with a wavevector perpendicular to $\boldsymbol{B}$, that the wavelength should be at a minimum 2 km in the zonal direction. This means that the minimum phase velocity in the radar frame is $V_{\rm ph} \geq 1.4\,{\rm Hz} \times 2000\,{\rm m} = 2800\,{\rm m/s}$.

The fractional Doppler shift for an observing velocity v_t relative to a reference frame containing a wave with phase velocity $V_{\rm PH}$ is

$$\frac{\omega'}{\omega} = 1 - \frac{v_t}{V_{\rm PH}}, \tag{18}$$

(which is derived from the substitution $x = x_0 + v_t t$ into the wave phase $\omega t - kx$.) From Fig. 1, the background electric field during the period of pulsations was 28 mV/m to the south, which gives an $\boldsymbol{E}\times\boldsymbol{B}$ drift velocity of roughly 550 m/s. Therefore, for a Doppler shift to the $\boldsymbol{E}\times\boldsymbol{B}$ frame we should take $v_t = 550$ m/s, and $V_{\rm PH} \geq 2800$ m/s. Putting these in Eq. (18) gives

$$0.8 \leq \frac{\omega'}{\omega} \leq 1.2. \tag{19}$$

Therefore, if we may represent the phenomena as a plane wave (i.e., a traveling wave with dependence of the form $\exp(i\omega t - ikx)$), the frequency associated with this phenomena in the plasma-fixed frame should be about the same as the frequency measured in the radar frame.

More generally, the phenomena may involve a wave packet, which can be represented as a sum of traveling waves of the form $\exp(i\omega t \pm ikx)$. In this case the restriction of Eq. (19) applies to each wave in the sum; so that, again, the Doppler shift should not have a large effect. For example, suppose that in the plasma reference frame there is a standing wave $\sin(\omega t - kx) + \cos(\omega t + kx)$. Then applying the transformation $x = x_0 + v_t t$ into the radar frame, and using trigonometric identities, we find that the wave observed in the radar frame is $[\sin(\omega t - kx_0) + \cos(\omega t + kx_0)]\cos(kv_t t) + [\cos(\omega t - kx_0) - \sin(\omega t + kx_0)]\sin(kv_t t)$. The terms in square brackets are standing waves of the same frequency and wavelength observed in the plasma frame. They are modulated by envelopes of frequency $\frac{kv_t}{2\pi} \leq \frac{550}{2000} = 0.28$ Hz, which is much less than the observed frequency of 1.4 Hz. That is, the observed frequency is much too high to be caused by the Doppler shift (the 0.28 Hz envelope), and must be due primarily to the oscillation frequency as it would be measured in the plasma frame (i.e., ω). In the case of a static drifting structure (i.e., $\omega = 0$ in the plasma frame), the frequency observed in the radar frame is just the envelope frequency, which we have just bounded as less than or equal 0.28 Hz.

The neutral wind velocity is typically less than 550 m/s. Hence, a similar analysis shows that Doppler shifting into the neutral wind reference frame, in which the E-region ions are stationary, also does not produce a significant Doppler shift.

In both cases, the Doppler shifting can only be substantial if the wavelength is somehow much shorter than as restricted above – i.e., as restricted by the spatial resolution of the measurement. Note that we can also argue against a short wavelength from the point of view that it is very difficult for precipitation to create the necessary sharp spatial structures, given that the AAR is drifting with the $\boldsymbol{E}\times\boldsymbol{B}$ drift, and the E-region plasma is drifting with the neutral wind; the precipitation would have to be both very narrow and very bursty.

4.2 Recombination-rate effects

The most notable pulsations evident in the optical images (Fig. 2a) have a frequency of 0.2 Hz – well below the frequency detected by the radar. However, there are also some faint pulsations with frequency 1.4 Hz, and which intersect beams 3 and 4; although they are most apparent 10 s to 20 s after the time of the radar detection, when their frequency is also a little higher (Sect. 3.5). Are these rapid modulations related to the radar observations, and if so, why are no 0.2 Hz pulsations seen in the radar data?

The pulsations seen in the optical images are caused by particle precipitation, which typically also causes ionization

of the neutral species, and hence plasma production. This source term is balanced by recombination, which has a rate proportional to the plasma density squared (n^2) (in the E-region). If the recombination time scale associated with the equilibrium plasma density is long compared to the pulsation period of the particle precipitation, then there is no time for the plasma density to drop significantly between pulsations, and there will be no significant oscillation of the plasma density. Figure 8 shows the recombination time constant derived from the plasma density measured by the radar, and from the MSIS model for the neutral density (Picone et al., 2002), using methods such as described by Semeter and Kamalabadi (2005). The detection of Fig. 6a was centered at an altitude of 130 km, which from Fig. 8 gives a recombination time constant (the time for the density to decay from n_0 to $\frac{n_0}{2}$) of $\tau_{\frac{1}{2}} = 10$ s. Specifically, it takes 10 s for the density to drop by 50%. The time between pulsations is only $\frac{1}{1.4\,\mathrm{Hz}} = 0.7$ s, which means that the density can only drop by about 1% between pulsations. Hence, even though the optical images show pulsations, there should be no significant modulation of the plasma density for the radar to detect. Above a certain frequency, modulation of the plasma density cannot be caused by modulation of particle precipitation.

In order to quantify the effects of periodic particle precipitation, we will solve the generation/recombination equation,

$$\frac{\mathrm{d}n}{\mathrm{d}t} = \alpha n_0^2(1+\xi\sin\omega t) - \alpha n^2, \tag{20}$$

for the plasma density n as a function of time. The production term $(\alpha n_0^2(1+\xi\sin\omega t))$ was chosen to make the root mean square plasma density equal to n_0, as can be verified by taking the mean of both sides of Eq. (20). When $\xi = 0$ the plasma reaches a steady state (i.e., $\frac{\mathrm{d}n}{\mathrm{d}t} = 0$) with $n = n_0$. Increasing ξ above zero adds a sinusoidal oscillation to the production term. In this case only the mean of $\frac{\mathrm{d}n}{\mathrm{d}t}$ is zero, i.e., $\left\langle \frac{\mathrm{d}n}{\mathrm{d}t} \right\rangle = 0$, and Eq. (20) gives $\sqrt{\langle n^2 \rangle} = n_0$.

Strictly speaking, Eq. (20) should be applied in the neutral wind reference frame, with zero electric field, so that the plasma is stationary. However, we have argued in the previous section that Doppler shifting to the radar reference frame will not substantially change the oscillation frequency.

We take $\xi = 1$ to give the maximum fractional modulation amplitude for sinusoidal fluctuations of the production term with frequency $\omega = 2\pi(1.4\mathrm{Hz})$, average steady state density $n_0 = 3\times10^{11}\,\mathrm{m}^{-3}$, and time constant $\tau_{\frac{1}{2}} = \frac{1}{(\alpha n_0)} = 10$s. (We must maintain $|\xi| \le 1$, because the production term cannot be negative.) Using all these values in Eq. (20), and solving with a numerical ODE solver starting from $n = 0$ at $t = 0$, gives the result shown in Fig. 8b.

Hence, we find that under the most favorable conditions (i.e., 100% source modulation), the expected plasma density modulation associated with the 1.4 Hz modulation of particle precipitation is only ±1.2%. However, the apparent density

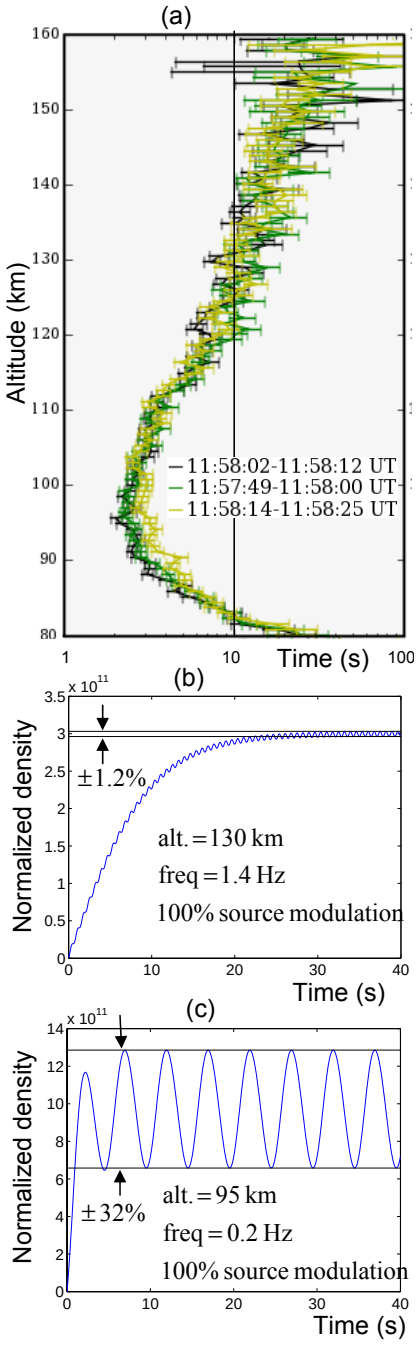

Fig. 8. **(a)** Recombination time scales from PFISR, **(b)** simulation of generation and recombination for 1.4 Hz signal, **(c)** simulation of generation and recombination for 0.2 Hz signal.

modulation indicated in Fig. 6 (or in Fig. 3) is around ±20%. (The time series in Figs. 3 and 6 are normalized.)

If the frequency is reduced to 0.2 Hz, the density modulation increases to ±7.8%. With our time sampling of 0.021 s, and for the 30 s duration of the 0.2 Hz pulsations, Eq. (12) gives an SNR of $10\log_{10}\left(0.078^2\left(\frac{30}{.021}\right)/4\right) = 3.4$ dB. This

is still below the lower limit of what might be considered a detectable signal.

Trying the 0.2 Hz frequency at a lower altitude of 95 km, which minimizes the recombination time constant, the density modulation increases to ±32%. This case is shown in Fig. 8c. With our time sampling of 0.021 s, and for the 30 s duration of the 0.2 Hz pulsations, Eq. (12) gives an SNR of $10\log_{10}\left(0.32^2\left(\frac{30}{.021}\right)/4\right) = 15.6$ dB. This is detectable. However, what this means is that it is detectable in the frequency domain, with a 30 s time series. Each data point in Fig. 2b has been averaged only 1/4 s, so that this signal would still appear very noisy in this time-domain plot.

The above analysis makes a number of additional assumptions, such as: (1) that there is no additive noise; (2) that the signal is a pure tone, with no frequency drift over the 30 s interval; and (3) that there is 100% modulation of the source. Any of these effects would decrease the SNR. Nevertheless, the fact that the same periodogram (frequency domain) processing used for the 1.4 Hz signal could not detect the 0.2 Hz signal may indicate that the precipitating particles were not deposited near 95 km.

In conclusion, the density effects of even the 0.2 Hz pulsations in particle precipitation, that are clearly observed in the keogram, possibly could not be detected by the radar; at least, it is not surprising that we do not observe them. With regard to 1.4 Hz periodic pulsations of the particle precipitation, they should not modulate the plasma density by more than one or two percentage points (at 130 km altitude). Such small density modulations should definitely not be detectable by ISR probing unless they persist for several minutes, without any change in frequency. Oscillations in the particle production cannot explain the ±20% modulation of the backscattered power time series, and the strong detector responses seen in Figs. 3 and 6. It seems necessary to ascribe these effects to another source.

5 Conclusions

Inertial Alfvén waves, or electromagnetic ion-cyclotron waves (which are Alfvén waves near the ion-cyclotron frequency), have been cited as the cause of "suprathermal" particle precipitation observed below the AAR (e.g., Johnstone and Winningham, 1982; Burch, 1991; Temerin et al., 1994; Chaston et al., 2000), as the source of large oscillating electric fields observed in the magnetosphere by satellites (e.g., Louarn et al., 1994; Stasiewicz et al., 1998; Chaston et al., 1999), and in the ionosphere by rockets (e.g., Boehm et al., 1990; Ivchenko et al., 1999), and as the source of flickering observed in the auroral brightness (e.g., Temerin et al., 1986; Sakanoi and Fukunishi, 2004; Sakanoi et al., 2005). Waves in the Pc 1 frequency range (0.2–5 Hz) may become resonant along magnetic field lines in a "cavity" bounded by the ionosphere and the AAR (the IAR), where they have wavelengths along the magnetic field of thousands to tens of thousands of kilometers. For waves in the inertial regime, which support a parallel electric field, and therefore can accelerate electrons (e.g., Hasegawa and Chen, 1975; Hasegawa, 1976; Goertz and Boswell, 1979; Lysak and Carlson, 1981; Ergun et al., 2005), the wavelength across the magnetic field ranges from less than a kilometer to a few tens of kilometers. Numerical simulations have found that for wavelengths less than about one kilometer the waves do not reflect off the ionosphere, when the ionosphere is treated as a fixed density profile, and therefore should not participate in the passive IAR phenomenon (Lessard and Knudsen, 2001). However, these waves support divergent perpendicular electric fields, which would cause divergent ion currents (Pedersen currents) if they reached the E-region ionosphere, in which case there would be density modulations. The density modulations should launch secondary Alfvén waves (Maltsev et al., 1977), which in theory can, under the right conditions, produce positive feedback and lead to unstable growth of the wave-electric fields and density modulations (the IFI). In addition, the deposition of electrons in the ionosphere creates a region of excess negative charge, and hence an inward-directed electric field, which causes an inward Pedersen current. Pedersen currents involve frictional heating (Joule heating) that may modulate the ion temperature, and hence the ISR back scatter from the auroral plasma. Can this broad picture of auroral Alfvén wave activity explain the radar observations?

We have argued that detectable 1.4 Hz density modulations could not have been caused by modulation of the auroral particle precipitation. Nevertheless, the CLVIS periodogram in Fig. 7a indicates modulation of the auroral precipitation at the same frequency, although this modulation is most evident a few seconds after the radar detection, when its frequency was a little higher (1.8 Hz). Despite these apparent offsets, it is tempting to conclude that the modulation of the radar back scatter is caused by a perpendicular Alfvénic electric field at the ionospheric altitude, and that the modulation of the optical emissions is caused by the acceleration of charged particles by the same (or closely related) Alfvén wave, traced back to the altitude of the AAR. However, there are at least two other mechanisms (other than Alfvén wave electric fields) by which the radar back scatter may be modulated: (1) the ambient electrons may be directly heated by collisions with precipitating charged particles (Rees, 1987); and (2) the deposition of charged particles may produce an excess of charge, and Joule heating from the currents flowing to neutralize this charge. What can we say about these alternative sources?

If heating mechanism number (1) (direct heating by collision with precipitating particles) were important, then it should have provided for ISR detection (in beams 6 and 7) of the 0.2 Hz pulsations that are seen so clearly in the optical data (Fig. 2a). Similarly, if heating mechanism number (2) (charge deposition) were important, then it also should have allowed for detection of the 0.2 Hz pulsations. In fact, if

modulation of the precipitation caused any detectable modulation of the ISR back scatter at 1.4 Hz, then it seems that the 0.2 Hz modulation should definitely have been detected. The fact that the 0.2 Hz pulsations were not detected is evidence that the 1.4 Hz detection was not caused by modulation of the auroral particle precipitation, through any mechanism. Hence, the result points to the presence of an electric field oscillation in the top side of the E-region ionosphere, which was not caused by particle precipitation.

From the fact that the detection was made in only two of five adjacent beams (Table 1), it appears that the region containing the 1.4 Hz pulsations extended only a few km in the meridional direction (or, that we happened to observe the southern edge of an extended structure). This would seem surprising given that in Sect. 4.1 we concluded that any horizontal wavelength must exceed about 2 km. It argues against the idea that the observed phenomena were produced by a plane-wave-like Alfvén wave packet. (By "plane-wave-like" we mean a packet that is locally, near its center, like a plane wave.) In addition, the radar evidence was from the top side of the E-region ionosphere. There is no evidence that the density depletions penetrated deeply into the ionosphere, as might be expected if there were a well developed feedback instability (i.e., the IFI) at play.

In conclusion, we want to sound a cautionary note. The radar and optical detections were not one to one; we have not established a conclusive relationship between them (Sect. 3.5). Also, the SNR for both detections was quite low. The main effect of this study should be to motivate additional ISR studies of Pc 1 band oscillations, in order to establish a pattern for the detections.

Appendix A

Theorem 9.1 from Kay (1998) states: Assume the data have the form $\boldsymbol{x} = \mathbf{H}\boldsymbol{\epsilon} + \boldsymbol{w}$, where $\mathbf{H}$ is a known $N \times p$ $(N > p)$ observation matrix of rank p, $\boldsymbol{\epsilon}$ is a $p \times 1$ vector of unknown signal-strength parameters, and $\boldsymbol{w}$ is an $N \times 1$ random Gaussian vector with zero mean and standard deviation σ. The GLRT for the hypothesis testing problem

$$\mathcal{H}_0 : \mathbf{A}\boldsymbol{\epsilon} = \boldsymbol{b} \qquad \text{(A1)}$$
$$\mathcal{H}_1 : \mathbf{A}\boldsymbol{\epsilon} \neq \boldsymbol{b}$$

where $\mathbf{A}$ is an $r \times p$ matrix $(r \leq p)$ of rank r, $\boldsymbol{b}$ is an $r \times 1$ vector, and $\boldsymbol{A\epsilon} = \boldsymbol{b}$ is a consistent set of linear equations, is to decide $\mathcal{H}_1$ if

$$T(\boldsymbol{x}) = \frac{N-p}{r} \frac{\left(\mathbf{A}\hat{\boldsymbol{\epsilon}} - \boldsymbol{b}\right)^T \left[\mathbf{A}\left(\mathbf{H}^T\mathbf{H}\right)^{-1}\mathbf{A}^T\right]^{-1}\left(\mathbf{A}\hat{\boldsymbol{\epsilon}} - \boldsymbol{b}\right)}{\boldsymbol{x}^T\left(\mathbf{I} - \mathbf{H}\left(\mathbf{H}^T\mathbf{H}\right)^{-1}\mathbf{H}^T\right)\boldsymbol{x}} > \gamma, \qquad \text{(A2)}$$

where $\hat{\boldsymbol{\epsilon}} = \left(\mathbf{H}^T\mathbf{H}\right)^{-1}\mathbf{H}^T\boldsymbol{x}$ is the maximum likelihood estimate of $\boldsymbol{\epsilon}$ under the $\mathcal{H}_1$ hypothesis.

For the case of detecting a sinusoidal signal of unknown phase we choose

$$\mathbf{H}_{n,(1,2)} = \left[\frac{1}{\sqrt{\Gamma}}\sin(\omega t_n - \alpha),\ \frac{1}{\sqrt{N-\Gamma}}\cos(\omega t_n - \alpha)\right], \qquad \text{(A3)}$$

which has dimension $N \times 2$ $(p = 2)$. The common phase α is chosen so that $\sum_{n=1}^{N}\sin(\omega t_n - \alpha)\cos(\omega t_n - \alpha) = 0$, which gives

$$\alpha = \frac{1}{2}\arctan\left[\frac{\sum_{n=1}^{N}\sin 2\omega t_n}{\sum_{n=1}^{N}\cos 2\omega t_n}\right]. \qquad \text{(A4)}$$

The normalization factors for $\mathbf{H}$ are

$$\Gamma = \sum_{n=1}^{N}\sin^2(\omega t_n - \alpha),\ N - \Gamma = \sum_{n=1}^{N}\cos^2(\omega t_n - \alpha). \qquad \text{(A5)}$$

With these choices $\mathbf{H}^T\mathbf{H} = \mathbf{I}_{2\times 2}$. The hypothesis testing problem involves determining if both the sin and cos components are zero, or not, and therefore we choose $\mathbf{A} = \mathbf{I}_{2\times 2}$ $(r = 2)$, and $\boldsymbol{b} = 0$. Substituting all these choices into Eq. (A2) gives Eq. (14).

Supplementary material related to this article is available online at: http://www.ann-geophys.net/28/1961/2010/angeo-28-1961-2010-supplement.zip.

The supplement contains a movie of the CLVIS images. The arrow points to the north. The circles show the locations of the 5 beams. The time shown is 26 s later than actual.

Acknowledgements. This material is based upon work supported by the National Science Foundation under Grant No. 0544750. Work at the Royal Institute of Technology was partially supported by the Swedish National Space Board. Thanks to Marc Lessard for Poker Flat magnetometer data and discussions of it. Thanks to Torsten Aslaksen for providing the guppy camera for the optical observations. Thanks also to Robert Michell and Marilia Samara for double checking the timing of the pulsations, and the existence of the rapid modulations.

Topical Editor K. Kauristie thanks G. Davidson and another anonymous referee for their help in evaluating this paper.

References

Atkinson, G.: Auroral arcs: Result of the interaction of a dynamic magnetosphere with the ionosphere, J. Geophys. Res., 75(25), 4746–4755, 1970.

Belyaev, P. P., Bosinger, T., Isaev, S. V., and Kangas, J.: First evidence at high latitude for the ionospheric Alfvén resonator, J. Geophys. Res., 104, 4305–4317, 1999.

Boehm, M. H., Carlson, C. W., McFadden, J. P., Clemmons, J. H., and Mozer, F. S.: High-resolution sounding rocket observations of large-amplitude Alfvén waves, J. Geophys. Res. 95, 12157–12171, 1990.

Burch, J. L.: Diagnosis of auroral acceleration mechanisms by particle measurements in Auroral Physics, edited by: Meng, C. I., Rycroft, M. J., and Frank, L. A., Cambridge Univ. Press, New York, 1991.

Chaston, C. C., Carlson, C. W., Peria, W. J., Ergun, R. E., and McFadden, J. P.: FAST observations of inertial Alfvén waves in the dayside auroral, Geophys. Res. Lett., 26(6), 647–650, 1999.

Chaston, C. C., Carlson, C. W., Ergun, R. E., and McFadden, J. P.: Alfvén waves, density cavities and electron acceleration observed from the FAST spacecraft, Phys. Scripta, T. 84, 64–68, 2000.

Chaston, C. C., Peticolas, L. M., Bonnell, J. W., Carlson, C. W., Ergun, R. E., McFadden, J. P., and Strangeway, R. J.: Width and brightness of auroral arcs driven by inertial Alfvén waves, J. Geophys. Res., 108(A2), 1091, doi:10.1029/2001JA007537, 2003.

Cosgrove, R. and Doe, R.: Effect of ionospheric depth on the ionospheric feedback instability: cutoff and subsequent $E_{\|}$ modes, Ann. Geophys., 28, 1777–1794, doi:10.5194/angeo-28-1777-2010, 2010.

Ergun, R. E., Andersson, L., Su, Y. J., Newman, D. L., Goldman, M. V., Lotko, W., Chaston, C. C., and Carlson, C. W.: Localized parallel electric fields associated with inertial Alfvén waves, Phys. Plasmas, 12, 072901, doi:10.1063/1.1924495g, 2005.

Farley, D. T.: Multiple-pulse incoherent-scatter correlation function measurements, Radio Sci., 7(6), 661–666, 1972.

Goertz, C. K. and Boswell, R. W.: Magnetosphere-Ionosphere Coupling, J. Geophys. Res., 84(A12), 7239–7246, 1979.

Hasegawa, A. and Chen, L.: Kinetic process of plasma heating due to Alfvén wave excitation, Phys. Rev. Lett., 35(6), 370–373, 1975.

Hasegawa, A.: Particle acceleration by MHD surface wave and formation of aurora, J. Geophys. Res., 81(28), 5083–5090, 1976.

Horne, J. H. and Baliunas, S. L.: A prescription for period analysis of unevenly sampled time series, Astrophys. J., 302, 757–763, 1986.

Ivchenko, N., Marklund, G., Lynch, K., Pietrowski, D., Torbert, R., Primdahl, F., and Ranta, A.: Quasiperiodic oscillations observed at the edge of an auroral arc by Auroral Turbulence 2, Geophys. Res. Lett., 26(22), 3365–3368, 1999.

Johnstone, A. D. and Winningham, J. D.: Satellite observations of suprathermal electron bursts, J. Geophys. Res. 87, 2321–2329, 1982.

Kay, S. M.: Fundamentals of statistical signal processing: Detection Theory, Prentis Hall Signal Processing Series, edited by: Oppenheim, A. V., 1998.

Lessard, M. R. and Knudsen, D. J.: Ionospheric reflection of small-scale Alfvén waves, Geophys. Res. Lett. 28(18), 3573–3576, 2001.

Lessard, M. R., Lund, E. J., Mouikis, C., Engebretson, M. J., and Mende, S. B.: Pi1B pulsations and Alfvénic aurora at substorm onset, AGU Fall Meeting, abstract #SM43D-01, 2006.

Louarn, P., Wahlund, J. E., Chust, T., de Feraudy, H., Roux, A., Holback, B., Dovner, P. O., Eriksson, A. I., and Holmgren, G.: Observation of kinetic Alfvén waves by the Freja spacecraft, Geophys. Res. Lett., 21, 1847–1850, 1994.

Lysak, R. L. and Carlson, C. W.: The effect of microscopic turbulence on magnetosphere-ionosphere coupling, Geophys. Res. Lett., 8, 269–272, 1981.

Lysak, R. L.: Coupling of the dynamic ionosphere to auroral flux tubes, J. Geophys. Res., 91(A6), 7047–7056, 1986.

Lysak, R. L.: Theory of Auroral zone Pi1B pulsation spectra, J. Geophys. Res., 93(A6), 5942–5946, June 1988.

Lysak, R. L. and Song, Y.: The Alfvénic aurora and substorm onset, AGU Fall Meeting, abstract #SM52A-05, 2008.

Maltsev, Y. P., Lyatsky, W. B., and Lyatskaya, A. M.: Currents over an auroral arc, Planet. Space. Sci., 25, 53–57, 1977.

Mende, S. B., Carlson, C. W., Frey, H. U., Immel, T. J., and Gérard, J.-C.: IMAGE FUV and in situ FAST particle observations of substorm aurorae, J. Geophys. Res., 108(A4), 8010, doi:10.1029/2002JA009413, 2003a.

Mende, S. B., Carlson, C. W., Frey, H. U., Peticolas, L. M., and Ostgaard, N.: FAST and IMAGE-FUV observations of a substorm onset, J. Geophys. Res., 108(A9), 1344, doi:10.1029/2002JA009787, 2003b.

Picone J. M., Hedin, A. E., Drob, D. P., and Aikin, A. C.: NRLMSISE-00 empirical model of the atmosphere: Statistical comparisons and scientific issues, J. Geophys. Res., 107, A12, doi:10.1029/2002JA009430, 2002.

Pokhotelov, O. A., Khruschev, V., Parrot, M., Senchenkov, S., and Pavlenko, V. P.: Ionospheric Alfvén resonator revisited: Feedback instability, J. Geophys. Res., 106(A11), 25813–25824, 2001.

Polyakov, S. V. and Rapoport, V. O.: The ionospheric Alfvén resonator, Geomag. Aeron., 21(5), 610–614, 1981.

Rees, M. H.: Modeling of the Heating and ionizing of the polar thermosphere by magnetospheric electron and ion precipitation, Phys. Scripta., T18, 249–255, 1987.

Sakanoi, T. and Fukunishi, H.: Temporal and spatial structures of flickering aurora derived from high-speed imaging photometer observations at Syowa Station in the Antarctic, J. Geophys. Res., 109, A01221, doi:10.1029/2003JA010081, 2004.

Sakanoi, T., Fukunishi, H., and Kasahara, Y.: A possible generation mechanism of temporal and spatial structures of flickering aurora, J. Geophys. Res., 110, A03206, doi:10.1029/2004JA010549, 2005.

Sato, N., Wright, D. M., Carlson, C. W., Ebihara, Y., Sato, M., Sato, M., Saemundsson, T., Milan, S. E., and Lester, M.: Generation region of pulsating aurora obtained simultaneously by the FAST satellite and a Syowa-Iceland conjugate pair of observatories, J. Geophys. Res., 109, A10201, doi:10.1029/2004JA010419, 2004.

Sato, T.: A theory of quiet auroral arcs, J. Geophys. Res., 83(A3), 1042–1048, 1978.

Semeter, J. and Kamalabadi, F.: Determination of primary electron spectra from incoherent scatter radar measurements of the auroral E region, Radio Sci., 40, 2, doi:10.1029/2004RS003042, 2005.

Stasiewicz, K., Holmgren, G., and Zanetti, L.: Density depletions and current singularities observed by Freja, J. Geophys. Res., 103, 4251–4260, 1998.

Streltsov, A. V. and Lotko, W.: Small-scale electric fields in downward auroral current channels, J. Geophys. Res., 108(A7), 1289, doi:10.1029/2002JA009806, 2003.

Streltsov, A. V. and Lotko, W.: Multiscale electrodynamics of the ionosphere-magnetosphere system, J. Geophys. Res., 109, A09214, doi:10.1029/2004JA010457, 2004.

Streltsov, A. V. and Lotko, W.: Coupling between density structures, electromagnetic waves and ionospheric feed-

back in the auroral zone, J. Geophys. Res., 113, A05212, doi:10.1029/2007JA012594, 2008.

Sulzer, M. P.: A phase modulation technique for a sevenfold statistical improvement in incoherent scatter data-taking, Radio Sci., 21(4), 737–744, 1986.

Temerin, M., McFadden, J., Boehm, M., and Carlson, C. W.: Production of flickering aurora and field-aligned electron flux by electromagnetic ion cyclotron waves, J. Geophys. Res., 91, 5769–5792, 1986.

Temerin, M., Carlson, C., and McFadden, J.: Auroral particle acceleration, Proceedings of the international conference on substorms-2., edited by: Kan, J. R., Craven, J. D., and Akasofu, S. I., p. 375, Univ. of Alaska, Fairbanks, 1994.

Trakhtengertz, V. Y. and Feldstein, A. Y.: Quiet auroral arcs: ionospheric effect on magnetosphere convection stratification, Planet. Space. Sci., 32(2), 127–134, 1984.

Vogt, J.: Alfvén wave coupling in the auroral current circuit, Surv. Geophys., 23, 335–377, 2002.

Whiter, D. K., Lanchester, B. S., Gustavsson, B., Ivchenko, N., Sullivan, J. M., and Dahlgren, H.: Small-scale structures in flickering aurora, Geophys. Res. Lett., 35, L23103, doi:10.1029/2008GL036134, 2008.